Rock Mechanics and Rock Engineering (2021) 54:1885–1896
https://doi.org/10.1007/s00603-020-02349-z

ORIGINAL PAPER

Modeling the Approach of Non-mated Rock Fracture Surfaces Under Quasi-static Normal Load Cycles

S. M. Rezaei Niya[1] · A. P. S. Selvadurai[1]

Received: 8 April 2020 / Accepted: 15 December 2020 / Published online: 30 January 2021

Abstract
This paper examines the quasi-static behaviour of a non-mated rock fracture during the first and second loading cycles. Asperity deformation, substrate deformation, asperity interaction and gouge production are included in the modelling. The composite topography assumption is revisited, and the irregular fracture topography is idealized by representing the asperities as ellipsoidal surfaces. It is shown that the modelling can capture the closure behaviour and hysteresis response of rock fractures on both the first and second loading–unloading cycles with an acceptable accuracy. The model is then used to examine sensitivity of deformation behaviours to mechanical properties. It is shown that Young's modulus of the rock is the most sensitive parameter with regard to the estimation of the closure behaviour of joints, followed by the compressive strength of the material, while the deformation is independent of the Poisson's ratio variations in the range of ± 0.1. Moreover, while the closure behaviour is sensitive to variations in the joint roughness coefficient on the first loading cycle, this sensitivity reduces considerably on the second cycle.

Keywords Closure behaviour · Normal stress · Rock fracture · Hysteresis · Sensitivity analysis

1 Introduction

Fractures commonly occur in rocks that have been subjected to mechanical action due to tectonic and geomorphological activity, underground construction and excavations. The performance of fractures is important to engineering activities associated with geologic disposal of hazardous wastes and greenhouse gases and hydraulic fracturing designed to extract geothermal energy and oil and gas resources. The hydro-mechanical performance of fractures and geological interfaces are, therefore, of major importance to engineering geosciences. The work in this area is extensive and a comprehensive review of the literature is beyond the scope of this article. The mechanical behaviour of geological interfaces has been reviewed in articles and volumes by Jaeger (1971), Barton and Choubey (1977), Barton and Stephansson (1990), Selvadurai and Boulon (1995), Nguyen and Selvadurai (1998), Selvadurai and Nguyen (1999), Selvadurai and Yu (2005), Misra and Huang (2012) and Selvadurai et al. (2015, 2018). Fluid transport in fractures and permeability evolution with stress is an extensively researched area and references to important contributions in this area are also given by Adler (1992), Boulon et al. (1993) and Selvadurai (2004, 2015) and Selvadurai and Głowacki (2017).

Fractures encountered in geologic media can be divided into two types; namely, mated or non-mated. In mated fractures, the two surfaces composing the fracture fit without any offset and the application of a stress normal to the nominal plane of the fracture induces progressive closure of the contacting surfaces. Mated fractures are rare but the regions comprising the fracture can experience relative motion largely induced by shear stresses that are applied to the nominal plane of the fracture. Depending on the stress state, the contacting surfaces can experience asperity degradation, gouge production and the continual evolution of the fluid transport characteristics (Nguyen and Selvadurai 1998). The non-mated fracture surfaces can result from relative movement along the nominal fracture plane. If the relative movement takes place in a low normal stress environment, the non-mated fracture surfaces can exhibit matched but translated surface profiles. The mechanical behaviour of non-mated fracture surfaces subjected to excess normal

✉ S. M. Rezaei Niya
seyed.niya@rmit.edu.au

[1] Department of Civil Engineering and Applied Mechanics, McGill University, 817 Sherbrooke West, Montreal, QC H3A 0C3, Canada

stresses is of interest to many areas in the geosciences; the closure of the aperture either by elastic deformation at the contacts, their failure and rupture and gouge development are topics that are also important to geomechanics. The mechanical behaviour of non-mated irregular fracture surfaces under compression is a complex problem in three-dimensional contact mechanics. This problem is best examined via computational approaches that can take into consideration (i) the elastic deformation of regions composing the non-mated fracture surfaces; (ii) the mechanics of contact at specific locations of the non-mated surfaces, which can involve three-dimensional, advancing, receding or stationary contacts in the presence of Coulomb friction, dilatant friction or finite friction; (iii) elastic–plastic or brittle fracture behaviour of the contacting surfaces that result in fragmentation and (iv) interaction of fragmented debris and the newly created fracture surfaces. To date, there are no mathematical approaches that can be effectively used to examine all these effects and computational approaches offer the only feasible approach for incorporating the variety of highly non-linear interactions at the contact zones (Aliabadi and Brebbia 1993; Willner 2003; Wriggers and Laursen 2007; Selvadurai and Atluri 2010; Selvadurai 2020).

The models describing the influence of normal stresses on non-mated fractures are categorized into three groups: empirical, numerical and theoretical (analytical) models (e.g., Marache et al. 2008; Tang et al. 2014, 2017; Kamali and Pournik 2016). Empirical models are normally non-linear mathematical functions fitted to measured closure behaviours of rocks (see e.g. Nguyen and Selvadurai, 1998; Marache et al., 2008; Tang et al. 2014). The measured joint closure behaviours reported by Bandis et al. (1983) and Barton et al. (1985) and the correlation presented between the joint roughness coefficient (JRC) and the stiffness and closure of the joints are important contributions in this category. While this category of models has the potential to predict the mechanical properties of specific fractures under predetermined normal loading, the generalization of the results towards a broader understanding of the phenomenon is not straightforward (Marache et al. 2008; Tang et al. 2014). There is no consensus on the definitions of the other two categories in the literature and the same models are categorized as theoretical or numerical models in different articles (e.g., compare the literature reviews in Marache et al. (2008), Tang et al. (2014), and Kamali and Pournik (2016)). In these categories, the model presented by Greenwood and Williamson using Hertzian contact theory (e.g., Popov 2010; Selvadurai and Glaser 2015, 2017) requires specific attention as it is the basis for later modified models (e.g., Pyrak-Nolte and Morris 2000; Marache et al. 2008; Tang et al. 2014, 2017; Kamali and Pournik 2016). This model (Greenwood and Williamson 1966) has been improved by other research groups who considered substrate deformation (e.g., Pyrak-Nolte and Morris 2000; Marache et al. 2008; Tang et al. 2014, 2017; Kamali and Pournik 2016), asperity interaction (e.g., Pyrak-Nolte and Morris 2000; Marache et al. 2008; Tang et al. 2017; Kamali and Pournik 2016), or gouge production and plastic deformation of asperities (e.g., Nguyen and Selvadurai 1998; Kamali and Pournik 2016). The asperities are often modeled as cylinders of various heights (e.g., Pyrak-Nolte and Morris 2000; Marache et al. 2008; Ameli et al. 2014; Kamali and Pournik 2016) on an elastic base; a variety of models that claim interaction between the asperities have been proposed and most of them show dubious consideration of the contact mechanics interactions between the idealized asperities and the elastic substrate. While the predicted closure behaviour of these models are generally in agreement (at least schematically) with measured closure behaviour of specific rocks for a limited range of loading (e.g., Marache et al. 2008; Tang et al. 2017; Kamali and Pournik 2016; Vogler et al. 2018), the hysteresis phenomenon has not been modeled or predicted. These results are significantly different from the closure behaviour of fractures in various rocks under loading and unloading conditions and also between successive loading–unloading cycles that have been reported in the literature (e.g., Bandis et al. 1983; Selvadurai 2015; Vogler et al. 2018).

The closure behaviour and deformation of rock joints and the above-mentioned hysteresis processes are studied using the 3D model presented in this paper. The fracture surfaces are reproduced using a compound method based on the JRC concept and self-affinity (Rezaei Niya and Selvadurai 2019). The asperities are modeled as ellipsoidal surfaces with their principal radii of curvature estimated from neighbouring points. The deformation of the asperities on the two surfaces of the fracture is analyzed separately and the composite topography assumption (Brown and Scholz 1985) is not employed for the reasons that will be explained in next section. The deformation of the asperities, substrate deformation and asperity interaction are considered. The equivalent stress is determined in each asperity and gouge production is modeled by assuming that the asperities are elastic-perfect brittle materials. It is shown that the predicted closure behaviour for various rock fractures for different loading–unloading cycles agrees with measured behaviours reported in the literature. The model is then used to analyze the sensitivity of the closure behaviour to variations in several mechanical properties of the rocks.

The theoretical analysis of the deformation of two in-contact ellipsoidal asperities on the upper and lower fracture surfaces is presented in next section. The algorithm developed for calculating the overall closure behaviour of a fracture is then discussed. The predicted behaviours are compared with the measured closure behaviour reported by Bandis et al. (1983). Finally, the sensitivity of the closure behaviour to variations in the Poisson's ratio, Young's

modulus, compressive strength, and JRC is analyzed for the first and second loading cycles. It is shown that the Young's modulus is the most dominant parameter controlling the closure behaviour of the analyzed fractures for both the first and second loading cycles.

2 Theory

To model the deformation of the fracture surface, the surface is discretized in a (mainly structured rectangular) grid and the coordinates of the upper and lower grid cells are normally summed to construct a composite topography (composite topography assumption; Brown and Scholz 1985; Fig. 1a versus Fig. 1b). These composite asperities are then considered as cylinders with various heights (Fig. 1b) and the elastic/plastic deformation of these cylinders is analysed (e.g., Pyrak-Nolte and Morris 2000; Marache et al. 2008; Kamali and Pournik 2016). This assumption, however, has the potential to model the surface geometries inaccurately. For example, interaction between two medium-height asperities is considered equivalent to the interaction of a tall asperity with a flat surface (compare the interactions shown in red and blue circles in Fig. 1). Also, the interactions between adjacent cells on the joint surfaces are ignored in modeling the asperities as cylinders. As an example, a peak surrounded by deep valleys is treated as a peak surrounded by other peaks (interactions marked by red and blue circles in Fig. 1). This can lead to erroneous results in the stress analysis. To resolve this issue, the asperities are modeled as ellipsoidal surfaces (see Fig. 1.c) where the principal radii of curvature are estimated from the elevations of neighbouring cells.

2.1 Deformation Analysis

Each joint surface is discretized using a structured rectangular 2D grid in the x–y plane (see Fig. 2). The height of each asperity (in z direction) is employed to estimate radii of curvatures in x and y directions. Two in-contact asperities on the upper and lower joint surfaces experiencing a normal force F are considered. For generality, different parameters are designated for the mechanical properties of the substrates and asperities (Young's modulus E, Poisson's ratio ν, compressive strength σ, and subscripts t, b, at, and ab for top substrate, bottom substrate, top asperity, and bottom asperity, respectively). Figure 2 shows the schematic view of the in-contact asperities (these asperities can, for example, be assumed to be those marked by a blue circle in Fig. 1.c).

Modelling the asperities as ellipsoidal surfaces, the principal radii of curvature of R_x (i.e., $R_{at,x}$, $R_{ab,x}$) and R_y (i.e., $R_{at,y}$, $R_{ab,y}$) are estimated by finding the radii of the circles passing

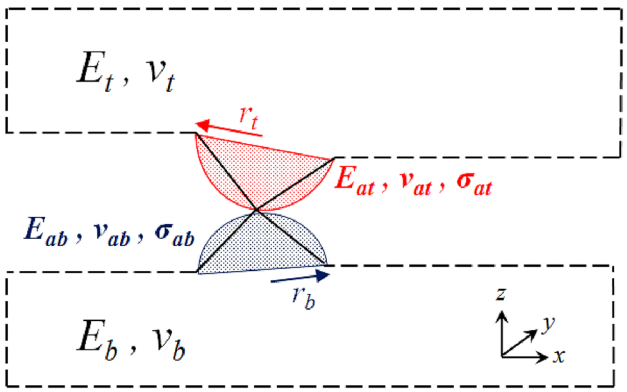

Fig. 2 The schematic view of in-contact asperities on the upper and lower surfaces

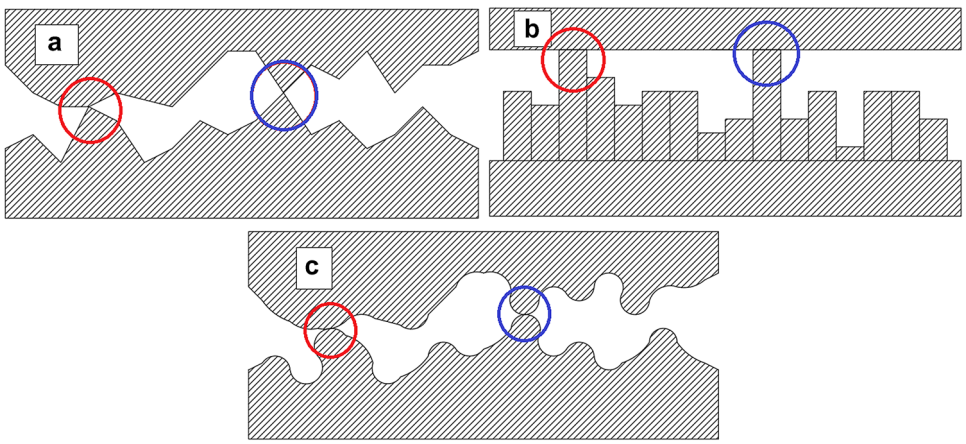

Fig. 1 **a** 2D representation of in-contact fracture surfaces and asperities. **b** Composite topography assumption; height of asperities at the upper and lower surfaces are added to construct cylinders to analyze the asperity interaction. **c** The method employed here; the asperities are modeled as ellipsoidal surfaces and the principal radii of curvature are estimated from the elevations of neighbouring cells; two specific asperity interactions are marked by red and blue circles to compare these different approaches

from the asperity and its neighbouring cells (see hatched areas in Fig. 2) in the x and y directions, respectively. The Gaussian radii of curvature for the asperities (R_{at}, R_{ab}) can then be determined as (Popov 2010)

$$R_{at} = \sqrt{R_{at,x}R_{at,y}}, \tag{1}$$

$$R_{ab} = \sqrt{R_{ab,x}R_{ab,y}}. \tag{2}$$

Based on Hertzian contact theory (Hertz 1882, see also Selvadurai 1979; Gladwell 1980; Johnson 1985; Aleynikov 2011; Selvadurai et al. 2018), the equivalent radius R_a and equivalent Young's modulus E_a^* for the asperities can be defined as

$$\frac{1}{R_a} = \frac{1}{R_{at}} + \frac{1}{R_{ab}}, \tag{3}$$

$$\frac{1}{E_a^*} = \frac{1-\nu_{at}^2}{E_{at}} + \frac{1-\nu_{ab}^2}{E_{ab}}. \tag{4}$$

The overall stiffness of the asperities (k_a) can then be calculated as

$$k_a = \frac{F}{\delta_a} = \frac{4}{3}E_a^* R_a^{1/2}\delta_a^{1/2}, \tag{5}$$

where F and δ_a are the applied normal force and overall deformation of the asperities, respectively. Assuming Hertz pressure applied to the base of the asperities, the stiffness of the upper and lower substrates can be determined as (Popov 2010)

$$k_t = \frac{F}{\delta_t} = \frac{4}{3}r_t E_t^*, \tag{6}$$

$$k_b = \frac{F}{\delta_b} = \frac{4}{3}r_b E_b^*. \tag{7}$$

In the above equations, r_t and r_b are the base radii of the top and bottom asperities, respectively (Fig. 2). Here, δ_t and δ_b are deformations of the upper and lower substrates and $E_t^* = E_t/(1-\nu_t^2)$ and $E_b^* = E_b/(1-\nu_b^2)$. Combining Eqs. (5–7), the substrate deformations (δ_t, and δ_b) can be determined from the overall deformation of the asperities (δ_a) as

$$\delta_t = \frac{E_a^*}{E_t^*}\frac{R_a^{1/2}}{r_t}\delta_a^{3/2}, \tag{8}$$

$$\delta_b = \frac{E_a^*}{E_b^*}\frac{R_a^{1/2}}{r_b}\delta_a^{3/2}. \tag{9}$$

The overall relative displacement of the surfaces resulting from one asperity contact (δ_S) can then be obtained as

$$\delta_S = \delta_a + \delta_t + \delta_b = \delta_a + \left(\frac{E_a^*}{E_t^*}\frac{R_a^{1/2}}{r_t} + \frac{E_a^*}{E_b^*}\frac{R_a^{1/2}}{r_b}\right)\delta_a^{3/2}. \tag{10}$$

If one assumes that the displacement δ_S is known (which is the case here in the solving algorithm explained in Sect. 3), the overall deformation of asperities δ_a (and therefore the substrate deformations δ_t and δ_b from Eqs. (8) and (9)) can be calculated analytically as

$$\delta_a = \left(\frac{-1}{3\gamma}(1+\Gamma+\frac{1}{\Gamma})\right)^2, \tag{11}$$

where

$$\gamma = \frac{E_a^*}{E_t^*}\frac{R_a^{1/2}}{r_t} + \frac{E_a^*}{E_b^*}\frac{R_a^{1/2}}{r_b}, \tag{12}$$

$$\Gamma = \sqrt[3]{\frac{2 - 27\gamma^2\delta_S \pm 3\gamma\sqrt{-81\gamma^2\delta_S^2 + 12\delta_S}}{2}}. \tag{13}$$

Even though the overall deformation of the asperities has been determined here, the individual deformations of the top and bottom in-contact asperities still need to be estimated. Assuming Hertzian contact conditions for both asperities, the equality of normal force on the asperities results in

$$\lambda = \frac{\delta_{at}}{\delta_{ab}} = \left(\frac{E_{ab}^*}{E_{at}^*}\right)^{2/3}\left(\frac{r_b}{r_t}\right)^{1/3}, \tag{14}$$

where δ_{at} and δ_{ab} are individual deformations of the top and bottom asperities, respectively. Also, $E_{at}^* = E_{at}/(1-\nu_{at}^2)$ and $E_{ab}^* = E_{ab}/(1-\nu_{ab}^2)$. Since $\delta_{at} + \delta_{ab} = \delta_a$, we have

$$\delta_{at} = \frac{\lambda}{1+\lambda}\delta_a, \tag{15}$$

$$\delta_{ab} = \frac{1}{1+\lambda}\delta_a. \tag{16}$$

While asperity and substrate deformations resulting from individual asperity contact between the upper and lower surfaces can be estimated using the above analysis, the displacements that occur due to asperity interaction also need to be considered. The vertical displacement at a point located at a distance ζ from the load center of a Hertz pressure for the top and bottom asperities can be determined as (Johnson 1985)

$$\delta_{\mathrm{int},t}(\zeta) = \frac{p_{0,t}}{2E_t^* r_t}\left[(2r_t^2 - \zeta^2)\sin^{-1}\left(\frac{r_t}{\zeta}\right) + r_t\sqrt{\zeta^2 - r_t^2}\right], \tag{17}$$

$$\delta_{\text{int},b}(\zeta) = \frac{p_{0,b}}{2E_b^* r_b}\left[(2r_b^2 - \zeta^2)\sin^{-1}\left(\frac{r_b}{\zeta}\right) + r_b\sqrt{\zeta^2 - r_b^2}\right], \tag{18}$$

where

$$p_{0,t} = \frac{2}{\pi}E_a^*\frac{R_a^{1/2}}{r_t^2}\delta_a^{3/2}, \tag{19}$$

$$p_{0,b} = \frac{2}{\pi}E_a^*\frac{R_a^{1/2}}{r_b^2}\delta_a^{3/2}. \tag{20}$$

For each asperity contact, the resulting asperity interaction needs to be calculated using these equations and considered in the analysis of other asperity contacts. The details will be explained in Sect. 3 that deals with the solving algorithm.

2.2 Stress Analysis

Considering the components of the contact stresses resulting from a Hertzian pressure distribution (Popov 2010), the equivalent stress according to the von Mises criterion (σ_V) along the z-axis (Fig. 2; z is measured from the point of contact) can be calculated as

$$\frac{\sigma_V}{p_{0,a}} = \frac{3}{2}\left(1 + \frac{z^2}{a^2}\right)^{-1} - (1+\nu)\left(1 - \frac{z}{a}\arctan\frac{a}{z}\right) \quad z \geq 0, \tag{21}$$

where a and ν are the contact radius and Poisson's ratio of the asperities, respectively. Here, $p_{0,a}$ is the pressure constant of the asperities and can be estimated as (Popov 2010)

$$p_{0,a} = \frac{2}{\pi}E_a^*\left(\frac{\delta_a}{R_a}\right)^{1/2}. \tag{22}$$

To improve computational efficiency of the analysis, Eq. (21) is evaluated numerically for different Poisson's ratios, and the maximum equivalent stress $(\sigma_V/p_{0,a})_{\max}$ and its coordinate $(z/a)_{\max}$ are determined. The results for the maximum equivalent stress as a function of Poisson's ratio are shown in Fig. 3. For each Poisson's ratio, the equivalent stress is obtained in different z/a values and the maximum value is reported in Fig. 3. The location of the maximum stress shifts from $z/a = 0.38$ at $\nu = 0$ to $z/a = 0.55$ at $\nu = 0.5$.

Figure 3 shows that the maximum equivalent stress can be estimated from Poisson's ratio using the following relationship:

$$\frac{\sigma_{V,\max}}{p_{0,a}} = 0.1251\nu^2 - 0.536\nu + 0.7695. \tag{23}$$

Assuming perfect brittle characteristics for asperities, an asperity is assumed to *break* when the maximum equivalent stress exceeds its compressive strength. Moreover, it is assumed that the asperity breaks such that its maximum equivalent stress becomes equal to its compressive strength. The details of these assumptions are again discussed in the solving algorithm in Sect. 3. While this model has to be considered as a simplified stress analysis of fractures, the results presented in the following sections show that it predicts the closure behaviour characteristics with an acceptable agreement with the measured closure behaviour given in the literature.

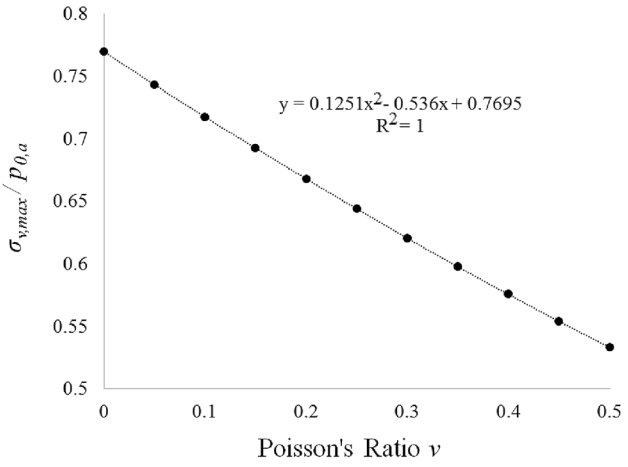

Fig. 3 The maximum equivalent stress as a function of Poisson's ratio as a result of a Hertzian pressure distribution

3 Solving Algorithm

To obtain the closure behaviour of a fracture under normal stress, the fracture surfaces must initially be reproduced. This process is discussed in Sect. 4. The upper and lower fracture surfaces are considered to be separated by a vertical distance such that the tallest overall asperity is in contact. The tallest overall asperity is assumed to be at a point where the algebraic sum of vertical coordinates (z direction in Fig. 2) of the upper and lower surfaces is a maximum. The solving algorithm consists of successive displacement steps until the overall force resulting from the summation of the asperity contact becomes equal to the applied normal force. In each displacement step, the maximum stress in each asperity is analyzed; the asperity *breaks* if the maximum stress becomes greater than the compressive strength of the asperity. The solution procedure is outlined in Fig. 4, while the details are explained as follows:

1. The vertical distance between the surfaces is reduced to the extent of one displacement step.
2. The in-contact asperities are detected and are sorted from the tallest overall asperity to the shortest one.

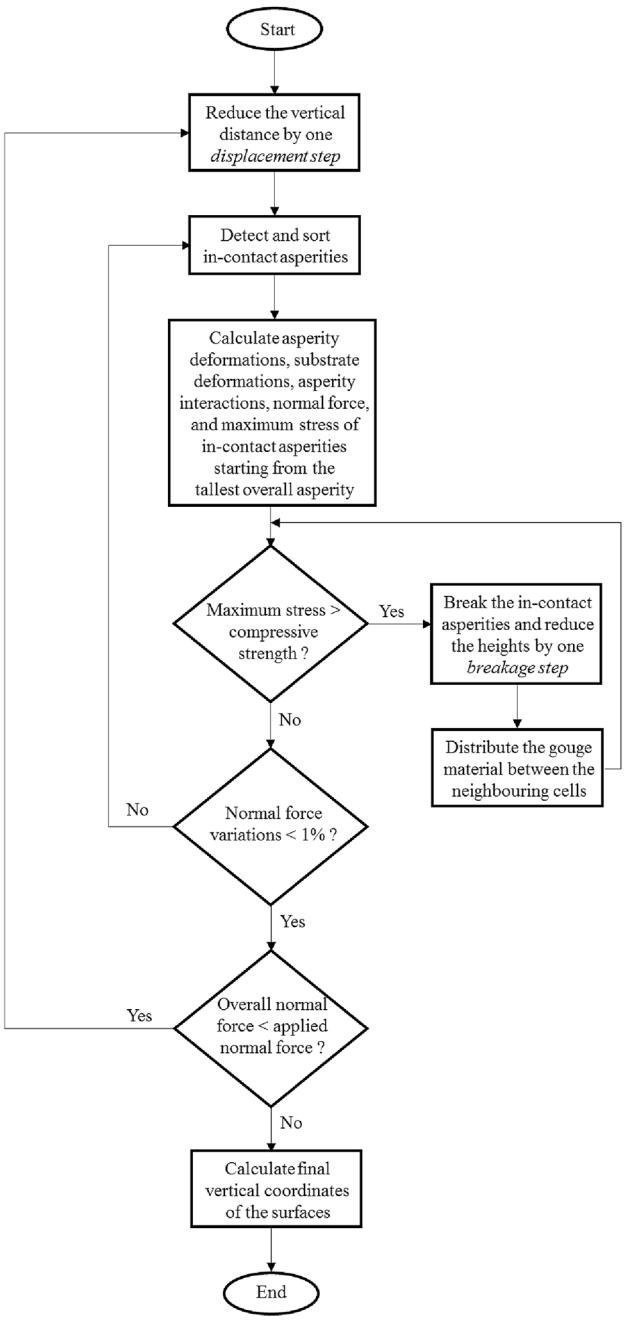

Fig. 4 Flowchart of the solution scheme

3. Starting from the tallest overall asperity, the asperity deformations (Eqs. (15) and (16)), the substrate deformations (Eqs. 8 and 9), the resulting vertical displacement at other asperity locations (i.e., asperity interaction, Eqs. 17 and 18), the normal force (Eq. 5), and the maximum equivalent stress of the asperity (Eq. 23) are calculated for each pair of in-contact asperities. At each step, the vertical coordinates of all the other asperities are corrected using the calculated vertical displacement.
4. If the maximum equivalent stress of one asperity becomes greater than the compressive strength of the asperity, the asperity breaks and the algorithm proceeds to step 2. The details of this breakage analysis are explained below.
5. It should be noted that the asperity interaction calculated here is one-sided. For example, the displacements of other asperities when the tallest overall asperity is in contact are considered; however, the effect of interaction of other in-contact asperities on the position and displacement of the tallest overall asperity is not analyzed. In this step, the algorithm proceeds to step 2 to consider all these asperity interactions. This loop (between step 5 and step 2) continues until the change of the calculated normal force in two successive calculations is less than 1% for all the asperities.
6. If the overall normal force that occurs due to asperity interaction is smaller than the applied normal force (calculated from the specified normal stress), the algorithm proceeds to step 1. Otherwise, the algorithm stops, and the final vertical coordinates of the upper and lower surfaces of the fracture are calculated by linearly interpolating the last two displacement steps, such that the overall normal force becomes equal to the applied normal force.

As mentioned in step 4, if the maximum equivalent stress in the in-contact asperities becomes greater than the compressive strength, the asperity is assumed to break. Assuming perfect brittle failure for the asperity, the process is modeled as follows:

1. The height of two in-contact asperities on the upper and lower fracture surfaces is reduced. The overall height reduction due to one breakage step is divided linearly between the upper and lower asperities according to the inverse of their ratio of radii of curvature; the larger the radius of curvature, the lower the share from the breakage step.
2. The gouge material resulting from this breakage is distributed by height to the neighboring grid cells (i.e., neighboring valleys) for each asperity. The height of the neighboring cells (valleys) is linearly increased according to their height difference with the broken asperity; the larger the difference, the greater the share of the gouge. The overall increment of the heights of the neighbouring cells is equal to the height decrement of the broken asperity. The radii of curvature for the asperities are updated according to the new heights.
3. Considering the new geometry, the maximum equivalent stress is re-calculated. If this stress is still greater than the compressive strength, the algorithm proceeds to step 1; otherwise, this breakage analysis is terminated.

The displacement and breakage steps have to be carefully selected since large steps can decrease the accuracy of the algorithm, while unreasonably small numbers can slow the algorithm performance considerably. Specifically, the breakage step has to be smaller than the displacement step. Here, a ratio of 0.4 is utilized.

The solving algorithm explained above, like other available models in the literature, ignores one important mechanism in the closure behaviour. When the vertical deformations of in-contact asperities on the upper and lower fracture surfaces under normal stress are analyzed, the possibility of horizontal displacements are ignored. When two in-contact asperities are under normal stress, they can easily escape the pressure by horizontal displacement towards adjacent valleys. This mechanism is especially efficient during lower normal loading when the taller asperities on the surfaces are in contact. The measured closure behaviours (e.g., see Fig. 5) also prove the importance of this mechanism. The data shows that there is always an *excess* deformation at low stresses (compared to high stresses), which will be preserved and reappear during the unloading process. This phenomenon can be traced in the next loading–unloading cycle as well, which suggests that there are *tall* asperities that are preserved during the loading and result in a considerable amount of vertical displacement at the lower stresses during the unloading process.

To resolve this issue, the detailed geometry of each asperity interaction has to be considered in deformation and stress analysis. While this *accurate* approach needs extensive computational resources, the *approximate alternative* is to fictitiously increase the flexibility of peaks by decreasing their Young's moduli. The idea of using lower Young's moduli for asperities has been reported in the literature before (e.g., Marache et al. 2008; Kamali and Pournik 2016; Bart et al. 2004; Newman and Elber 1988; Shi and Durucan 2016). Marache et al. (2008) stated that asperities are likely to be

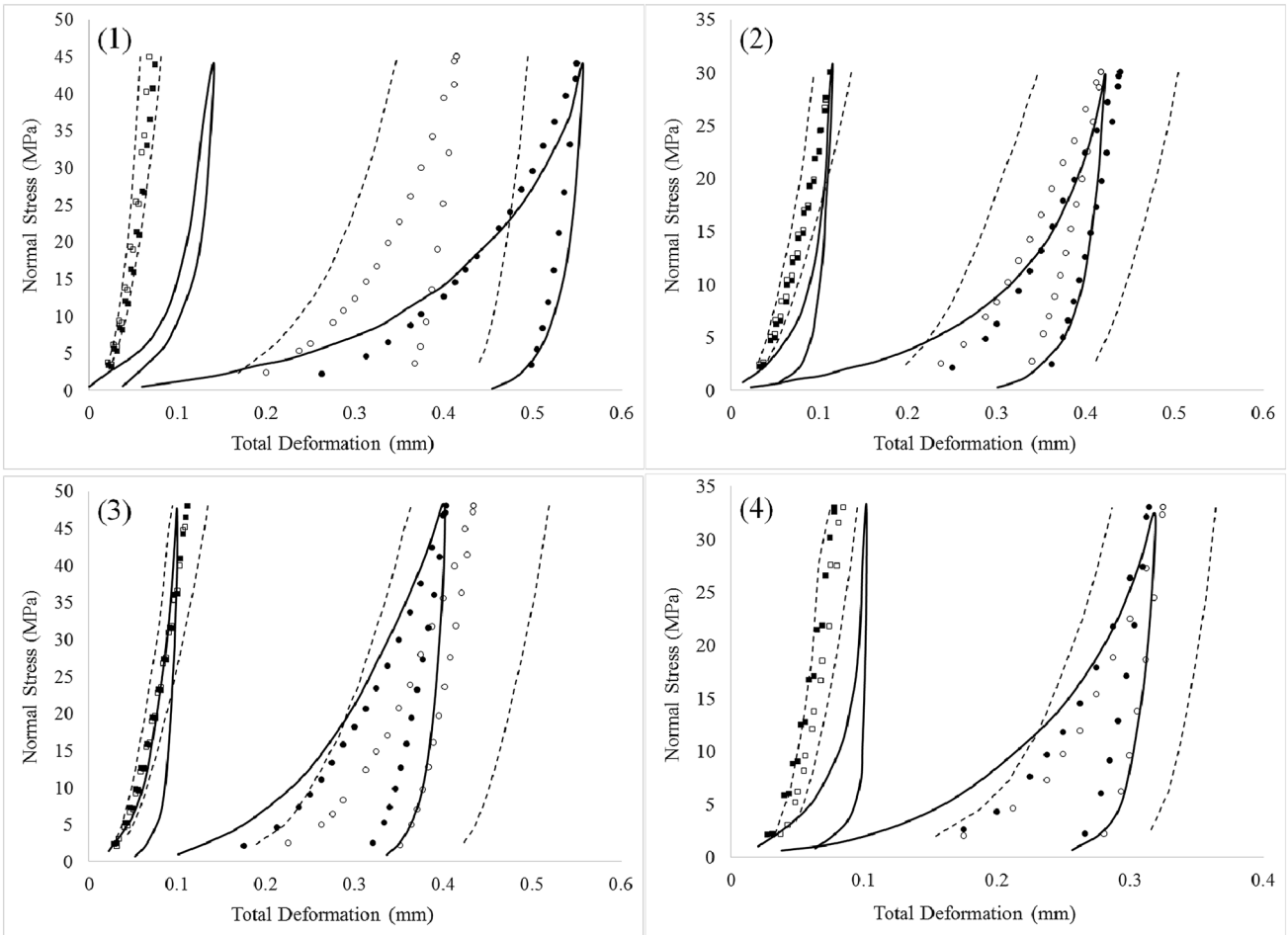

Fig. 5 Closure behavior of the samples presented in Table 1: —— Experimental results for the first and second cycles (Bandis et al. 1983); ○ closest result to the average of modeling results for first cycle; □ modeling result of second loading–unloading cycle for the closest result to the average; ● best fit from modeling results to the measured behaviour for first cycle; ■ best fit from modeling results to the measured behaviour for second cycle; - - - one standard deviation ranges from average of modeling results

weaker than the surrounding rocks because of geologic processes, such as fluid flow through the fractures. The difference between the Young's moduli of intact rocks and asperities has also been related to the corrosion process and products (Newman and Elber 1988). It is worth mentioning that considering the local heterogeneity of rocky materials, fractures occur at the stiffer points (i.e., a higher Young's moduli) under a constant displacement assumption. In other words, the locally softer zones (i.e., with a lower Young's moduli) remain connected to the substrate and become the asperity peaks. Here, the ratio of Young's moduli of the peaks to the substrates is considered to be 0.05, which is the middle point of the reported ranges (Shi and Durucan 2016; Newman and Elber 1988). A peak is defined here as the point that has a higher elevation than all the surrounding points.

4 Reproduction of Fracture Surfaces

The fracture surfaces are reproduced here using the compound algorithm presented recently by Rezaei Niya and Selvadurai (2019). The algorithm reproduces a 3D fracture surface using both the JRC and the fractal dimension. The recent literature on fracture surface reproduction was reviewed in Rezaei Niya and Selvadurai (2019) who suggested that the JRC is a reasonable parameter to quantify the roughness of the fracture surface for practical purposes. It is quite straightforward to measure the JRC of a fracture in both laboratory and field environments. The measured JRC is an average of several tests and is independent of normal stress under a wide range of applied stresses (Barton and Choubey 1977; Rezaei Niya and Selvadurai 2019). However, it is more accurate to present a *range* (rather than a specific number) for the JRC for fractures in a specific rock (Rezaei Niya and Selvadurai 2019).

The reliability of the compound algorithm was discussed and verified by Rezaei Niya and Selvadurai (2019). It was shown that the reproduced 3D fracture surfaces can be considered as a reliable extension of the standard 2D JRC profiles presented by Barton and Choubey (1977). It should be noted that since the algorithm uses a random value for local slopes of the surface profiles, it gives unlimited visualizations of the fracture surfaces for a constant JRC value. Therefore, the closure behaviour study for the fractures reproduced here requires some statistical analysis. Moreover, the upper and lower fracture surfaces are reproduced independently here to model non-mated fractures. While translated surfaces clearly react differently than independent surfaces (as long as translation is less than the shifting threshold, Rezaei Niya and Selvadurai 2019), the closure behaviour occurring during the translation process is not analyzed here. It was shown that surface translations greater than 160 times the aperture size result in independent surfaces (Rezaei Niya and Selvadurai 2019). However, this threshold is estimated based on fracture permeability analysis and needs to be re-evaluated for closure behaviour analysis.

Here, a 100×100 mesh size with a cell size of 0.25 mm is employed to reproduce the fracture surfaces (see also Rezaei Niya and Selvadurai 2019). The displacement and breakage steps are assumed as 12.5 and 5 microns for the first loading process and 6.25 and 2.50 microns for the first unloading and second loading/unloading cycle. For each cell, the radii of curvature are determined from the heights of the cell and the neighboring cells in the x and y directions.

5 Verification of the Modeling Results

To analyze the accuracy of the presented algorithm, the closure behaviour of the fractures in four different sample rocks measured and reported by Bandis et al. (1983) are modeled here. The details of the mechanical properties used for the modeling are presented in Table 1. The measured closure behaviour for weathered joints is considered here since it is expected to better represent the independent surfaces assumption used in the modeling analysis.

The fracture closure results are shown in Fig. 5. In each case, 20 different samples of the fractures were produced, and the closure behaviour analyzed. The closest result to the average value, one standard deviation range, and the best fit to the experimental results between the samples for the first

Table 1 Mechanical properties of the samples used for model verification analysis (Bandis et al. 1983)

Sample number	Rock materials	Joint roughness coefficient (JRC)	Young's modulus E (GPa)	Compressive strength σ (MPa)	Poisson's ratio ν
1	Dolerite	8[a]	78[a]	165[a]	0.2[2]
2	Siltstone	7[a]	28.5[a]	84[a]	0.25[c]
3	Limestone	8[a]	49[a]	152[a]	0.2[c]
4	Slate	6.5[a]	66[a]	159[a]	0.25[b]

[a]Bandis et al. (1983)

[b]Ivars et al. (2011), Augustinus and Selby (1990)

[c]Gercek (2007)

and second loading–unloading cycles are shown. The figure shows that the model is able to capture the closure behaviour of the first and second loading–unloading cycles for different rock samples with a reasonable accuracy. The disconnectedness of the hystereses is due to the convention employed in the experimental results (Bandis et al. 1983).

The average of the modeling results has the highest discrepancy with the measured values for sample 1 (dolerite). However, even in this case, there is one modeling result (between the 20 samples analyzed) that has an acceptable agreement with the measured behaviour for the first cycle. The predictions for the second cycle behaviour for this sample were less accurate than for the other samples; this requires more analysis in future works. The predicted behaviour for the second cycles is, in general, less accurate than for the first loading/unloading cycles. As can be seen in Fig. 5 and discussed previously in Sect. 3, there is *excessive* deformation at lower stresses for both the first and second cycles in measured behaviours. The model was not capable of capturing this behaviour for the second loading cycles, especially for rock samples 1 and 4. This inability could be the result of using a lower Young's moduli for the asperities instead of accurately modeling the horizontal displacements.

6 Sensitivity Analysis of Closure Behaviour

In this section, the sensitivity of the closure behaviour to the variations of Poisson's ratio, Young's modulus, compressive strength, and JRC is analysed. Indifference intervals for these parameters are calculated first. The indifference interval is defined as the range in which the variations of an analyzed parameter (e.g., Poisson's ratio) did not result in statistically significant variations of the target parameter (here, total deformation) (Rezaei Niya et al. 2016; Montgomery 2009). For the analysis presented in this section, the closure behaviour of each sample given in Table 1 is analyzed by increasing/decreasing one of its mechanical properties in each study. The analyzed cases are shown in Table 2. For each case, 20 different samples of the fractures were reproduced and analyzed. The sensitivity analyses were performed only for the maximum normal stress (maximum deformation) points here. The analysis to determine the indifference interval for Poisson's ratio is presented in the following. Indifference intervals for the other parameters can be determined in a similar manner.

A second-order correlation between the average of maximum deformations in 20 simulations, $x_{\max}$, and Poisson's ratio ν is assumed. Since three data points are available for each case (two points with higher/lower Poisson's ratios from Table 2 and one point with the correct Poisson's ratio from Table 1), this is the most general possible assumption. The correlation can also be written in the form of a Taylor expansion about $\nu = \nu_M$; however, it is not expected to improve the accuracy level since a similar second-order correlation will be developed.

$$x_{\max} = b\nu^2 + c\nu + d, \tag{24}$$

where b, c, and d are second-order correlation coefficients. These coefficients can be determined from the three data points:

$$\begin{cases} b\nu_H^2 + c\nu_H + d = x_{\max,\nu H} \\ b\nu_M^2 + c\nu_M + d = x_{\max,\nu M} \\ b\nu_L^2 + c\nu_L + d = x_{\max,\nu L} \end{cases}. \tag{25}$$

Here, ν_H and ν_L are the higher and lower Poisson's ratios from Table 2 (e.g., for sample 1, they are 0.3 and 0.1, respectively). ν_M is the Poisson's ratio of the sample from Table 1 (e.g., 0.2 for sample 1), and $x_{\max,\nu H}$, $x_{\max,\nu L}$, and $x_{\max,\nu M}$ are the corresponding averages of maximum deformations for the higher, lower, and real Poisson's ratios, respectively. Assuming a similar correlation for the standard deviation of the maximum deformation,

$$S_{x\max} = b_s\nu^2 + c_s\nu + d_s, \tag{26}$$

the corresponding correlation parameters can be similarly calculated.

$$\begin{cases} b_s\nu_H^2 + c_s\nu_H + d_s = S_{x\max,\nu H} \\ b_s\nu_M^2 + c_s\nu_M + d_s = S_{x\max,\nu M} \\ b_s\nu_L^2 + c_s\nu_L + d_s = S_{x\max,\nu L} \end{cases}. \tag{27}$$

For an arbitrary point $x_{\max}(\nu)$ with a standard deviation of $S_{x\max}(\nu)$, the t test value can be determined as (Montgomery 2009)

Table 2 The analyzed cases for sensitivity analysis

Sample number	Joint roughness coefficient (JRC)		Young's modulus E (GPa)		Compressive strength σ (MPa)		Poisson's ratio ν	
1	6	10	70	85	150	180	0.1	0.3
2	5	9	25	32	75	93	0.15	0.35
3	6	10	45	53	137	167	0.1	0.3
4	5	8	60	72	143	175	0.15	0.35

$$t_0 = \frac{x_{\max}(\nu) - x_{\max,\nu M}}{\sqrt{\frac{S^2_{x\max}(\nu) + S^2_{x\max,\nu M}}{20}}}. \tag{28}$$

There is a statistically significant variation in $x_{\max}(\nu)$ when $|t_0|$ becomes greater than $t_{cr} = 2.025$ for a significance level of 0.05 (Montgomery 2009). Inserting Eqs. (24) and (26) into Eq. (28) results in

$$\begin{aligned}&\left(20b^2 - t^2_{cr}b^2_s\right)\nu^4 + \left(40bc - 2t^2_{cr}b_sc_s\right)\nu^3 + \left(20c^2 + 40b(d - x_{\max,\nu M}) - t^2_{cr}c^2_s - 2t^2_{cr}b_sd_s\right)\nu^2 \\ &+\left(40c(d - x_{\max,\nu M}) - 2t^2_{cr}c_sd_s\right)\nu + \left(20(d - x_{\max,\nu M})^2 - t^2_{cr}(d^2_s + S^2_{x\max,\nu M})\right) = 0.\end{aligned} \tag{29}$$

The closest real solution of the above equation to ν_M indicates the smallest change in ν that results in a t test value of t_{cr} (i.e., presented definition for the indifference interval). As an example, the closest real solution of this equation to $\nu_M = 0.2$ for sample no. 1 (dolerite) for the first loading cycle is 0.060; this means that changes smaller than 0.140 in the Poisson's ratio result in t test values smaller than t_{cr}. As a result, the effect of Poisson's ratio variations smaller than 0.140 on the maximum deformation is statistically negligible; in other words, the length of the indifference interval for Poisson's ratio for sample no. 1 for the first loading cycle can be estimated as 0.140.

Analyses can be performed to estimate the length of the indifference intervals for Poisson's ratio, Young's modulus, compressive strength, and the JRC for the first and second loading cycles for all four samples. The results of this analysis are tabulated in Table 3, which shows the percentage of indifference variations in each case. The roots of Eq. (29) are all complex numbers for the three cases where no values are presented in Table 1. When the standard deviation of the maximum deformation ($S_{x\max,\nu M}$) is not large enough, the equation will not have any real solution.

The effect of the mechanical properties of the examined rocks on their closure behaviour can be analyzed using the data presented in Table 3. The table specifically shows that Poisson's ratio has the lowest effect on the closure behaviour of the analyzed joints for both the first and second loading cycles. The closure behaviour can be safely assumed to be independent of Poisson's ratio variations in the range of ± 0.1. On the other hand, Young's modulus is the parameter that has the greatest influence on the closure behaviour analysis; small variations in the Young's modulus will affect the maximum deflection of the joints. This sensitivity is significantly increased on the second loading cycle. The maximum deflection on the second loading cycle is continuously increased for all cases when the Young's modulus is decreased (data not shown here).

The compressive strength is the next sensitive parameter that has an influence on joint closure behaviour. The maximum deflection is even more sensitive to the compressive strength variations on the second loading cycle where a 5% variation in compressive strength results in a statistically different maximum deflection. The results (not shown here) show that the maximum deflection on the second loading cycle increases for all the cases as the compressive strength increases. Finally, the sensitivity of the maximum deflection to the JRC changes considerably from the first loading cycle to the second loading cycle. While closure behaviour statistically varies for variations of ± 1 JRC for the first loading, the sensitivity for the second loading decreases up to ± 3 JRCs for rock samples 3 and 4. The results (not shown here) also show that while the maximum deflection decreases for all the cases studied for the first loading cycle when the JRC decreases, this trend is not found for the second loading cycle.

Table 3 The length of indifference intervals for various mechanical properties of the samples presented in Table 1

	First loading cycle				Second loading cycle			
Sample No	1	2	3	4	1	2	3	4
Poisson's ratio ν	0.140 (70%)	0.0990 (40%)	–	–	0.187 (94%)	0.0923 (37%)	0.121 (60%)	0.0752 (30%)
Young's modulus E (GPa)	12.7 (16%)	3.93 (14%)	–	7.38 (11%)	3.49 (4.5%)	0.733 (2.6%)	1.28 (2.6%)	2.01 (3.0%)
Compressive strength σ (MPa)	27.7 (17%)	8.64 (10%)	19.8 (13%)	65.1 (41%)	12.2 (7.4%)	4.51 (5.4%)	6.90 (4.5%)	5.15 (3.2%)
Joint roughness coefficient (JRC)	0.908 (11%)	0.948 (14%)	1.31 (16%)	0.726 (11%)	1.46 (18%)	1.99 (28%)	3.29 (41%)	3.18 (49%)

The percentage of indifference variations is also given for each case

7 Conclusions

Closure behaviour of a non-mated rock fracture under normal loading on the first and second loading–unloading cycles is modeled in this paper. Asperity and substrate deformation and asperity interactions are theoretically analyzed. The equivalent stress in the asperities is estimated and gouge production is determined. The deformation and gouge-production modeling algorithms and fracture surface reproduction method are presented. The model is then verified using the measured closure behaviour of fractures in four types of rocks reported in the literature. For each case, 20 samples of the rock fracture are produced, and the closure behaviour is analyzed. It is shown that the model can estimate the closure behaviour of fractures for the first and second loading–unloading cycles with an acceptable accuracy. The model is then employed to analyse the sensitivity of the closure behaviour to various mechanical properties of rocks. It is shown that Young's modulus is the most dominant parameter controlling the deformation behaviour of fractures on both the first and second loading cycles, and Poisson's ratio has the least effect on the closure behaviour. The maximum deflection of the fracture under constant normal stress on the second loading cycle is increased when Young's modulus is decreased, and/or the compressive strength is increased.

It has to be emphasized that the accuracy of the observations reported in this paper is bounded by the accuracy of assumptions employed in the analysis. Specifically, the following assumptions need special considerations: (i) the model developed for the closure behaviour analysis presented in Sects. 2 and 3 is assumed to be accurate for both the first and second loading cycles; more elaborate models can be developed to improve the accuracy level of the analysis (e.g., by considering relative translation and/or rotation of the surfaces). Also, the reproduction algorithm for fracture surfaces reviewed in Sect. 4 and the assumptions employed in this process could affect the accuracy level of the results. (ii) The fracture surfaces were reproduced independently here (i.e., the apertures on upper and lower surfaces of the fracture are not spatially correlated); the accuracy of this assumption under various field and experimental conditions needs to be considered in the analysis. (iii) The sensitivity analysis performed here is only based on the maximum deflection of the non-mated fracture under normal stress and the stress-deformation curves were not analyzed. Analyzing such curves could result in a better understanding of the phenomenon. (iv) The sensitivity analysis is based on the estimation of the maximum deformation as a second-order function of the analyzed parameter (e.g., Poisson's ratio). While this estimation is the most general possible assumption of the available three data points, the accuracy level of this assumption can affect the accuracy of the sensitivity results. (v) The analyses were carried out under the predetermined normal stresses employed and reported in Bandis et al. (1983). Further analysis is required to investigate whether the results are independent of the normal stress employed. (vi) As mentioned in Sect. 4, it is more accurate to consider a *range* (rather than a specific number) for the JRC value of a fracture. Also, the assumption that the JRC is independent of the normal stress is more accurate when a JRC *range* is considered. However, the insensitivity of maximum deflection to JRC variations for the second loading cycle supports the assumption that a JRC *range* will be independent of the applied normal stresses.

Compliance with Ethical Standards

Conflict of interest The authors declare that they have no conflict of interest.

References

Adler PM (1992) Porous media: geometry and transports. Butterworth-Heinemann, London

Aleynikov SM (2011) Spatial contact problems in geotechnics-boundary element method. Springer-Verlag, Berlin

Aliabadi M, Brebbia CA (1993) Computational methods in contact mechanics. Computational Mech Publ, Southampton

Ameli P, Elkhoury JE, Morris JP, Detwiler RL (2014) Fracture permeability alteration due to chemical and mechanical processes: a coupled high-resolution model. Rock Mech Rock Eng 47:1563–1573

Augustinus PC, Selby MJ (1990) Rock slope development in McMurdo Oasis, Antarctica, and implications for interpretations of glacial history. Geographysika Annalen A 72:55–62

Bandis SC, Lumsden AC, Barton NR (1983) Fundamentals of rock joint deformation. Int J Rock Mech Min Sci Geomech Abstr 20:249–268

Bart M, Shao JF, Lydzba D, Haji-Sotoudeh M (2004) Coupled hydro-mechanical modeling of rock fractures under normal stress. Can Geotech J 41:686–697

Barton N, Choubey V (1977) The shear strength of rock joints in theory and practice. Rock Mech 10:1–54

Barton N, Stephansson O (1990) Rock joints. In Proceedings of the International Symposium on Rock Joints. Loen: AA Balkema

Barton N, Bandis S, Bakhtar K (1985) Strength, deformation and conductivity coupling of rock joints. Int J Rock Mech Min Sci Geomech Abstr 22:121–140

Boulon MJ, Selvadurai APS, Benjelloun H, Feuga B (1993) Influence of rock joint degradation on hydraulic conductivity. Int J Rock Mech Min Sci Geomech Abstr 30:1311–1317

Brown SR, Scholz CH (1985) Closure of random elastic surfaces in contact. J Geophys Res 90:5531–5545

Gercek H (2007) Poisson's ratio values for rocks. Int J Rock Mech Min Sci 44:1–13

Gladwell GML (1980) Contact problems in the classical theory of elasticity. Sijthoff & Noordhoff, The Netherlands

Greenwood JA, Williamson JP (1966) Contact of nominally flat surfaces. P Roy Soc Lond A Mat 295:300–319

Hertz H (1882) Uber die Beruhrung fester elastischer Korper. J fur die Reine Angewandte Mathematic 92:156–171
Ivars DM, Pierce ME, Darcel C, Reyes-Montes J, Potyondy DO, Young RP, Cundall PA (2011) The synthetic rock mass approach for jointed rock mass modelling. Int J Rock Mech Min Sci 48:219–244
Jaeger JC (1971) Friction of rocks and stability of rock slopes. Geotechnique 21:97–134
Johnson KL (1985) Contact mechanics. Cambridge University Press, Cambridge
Kamali A, Pournik M (2016) Fracture closure and conductivity decline modeling—application in unpropped and acid etched fractures. J Unconventional Oil Gas Res 14:44–55
Marache A, Riss J, Gentier S (2008) Experimental and modelled mechanical behaviour of a rock fracture under normal stress. Rock Mech Rock Engng 41:869–892
Misra A, Huang S (2012) Micromechanical stress-displacement model for rough interfaces: Effect of asperity contact orientation on closure and shear behaviour. Int J Solids Structures 49:111–120
Montgomery DC (2009) Design and analysis of experiments. John Wiley & Sons, New Jersey
Newman JC, Elber W (1988) Mechanical of fatigue crack closure. ASTM, Philadelphia
Nguyen TS, Selvadurai APS (1998) A model for coupled mechanical and hydraulic behaviour of a rock joint. Int J Numer Anal Met 22:29–48
Popov VL (2010) Contact mechanics and friction. Springer-Verlag, Berlin, Physical principles and applications
Pyrak-Nolte LJ, Morris JP (2000) Single fractures under normal stress: the relation between fracture specific stiffness and fluid flow. Int J Rock Mech Min Sci 37:245–262
Rezaei Niya SM, Selvadurai APS (2019) Correlation of joint roughness coefficient and permeability of a fracture. Int J Rock Mech Min Sci 113:150–162
Rezaei Niya SM, Phillips RK, Hoorfar M (2016) Sensitivity analysis of the impedance characteristics of proton exchange membrane fuel cells. Fuel Cells 16:547–556
Selvadurai APS (1979) Elastic analysis of soil-foundation interaction. Elsevier, Amsterdam
Selvadurai APS (2004) Stationary damage modelling of poroelastic contact. Int J Solids Struct 41:2043–2064
Selvadurai APS, Atluri SN (eds) (2010) Contact mechanics in the engineering sciences. Tech Science Press, GA
Selvadurai APS (2015) Normal stress-induced permeability hysteresis of a fracture in a granite cylinder. Geofluids 15:37–47
Selvadurai APS (2020) In-plane loading of a bonded rigid disc embedded at a pre-compressed elastic interface: the role of non-linear interface responses. Mech Syst Signal Processing 144:106871. https://doi.org/10.1016/j.ymssp.2020.106871
Selvadurai APS, Boulon MJ (1995) Mechanics of geomaterial interfaces, Studies in applied mechanics, vol 42. Elsevier, Amsterdam
Selvadurai PA, Glaser SD (2015) Laboratory-developed contact models controlling instability on frictional faults. J Geophys Res 120:4208–4236
Selvadurai APS, Głowacki A (2017) Stress-induced permeability alterations in an argillaceous limestone. Rock Mech Rock Eng 50:1079–1096
Selvadurai APS, Nguyen TS (1999) Mechanics and fluid transport in a degradable discontinuity. Eng Geol 53:243–249
Selvadurai APS, Yu Q (2005) Mechanics of a discontinuity in a geomaterial. Comput Geotech 32:92–106
Selvadurai APS, Suvorov AP, Selvadurai PA (2015) Thermo-hydro-mechanical processes in fractured rock formations during a glacial advance. Geosci Model Dev 8:2167–2185
Selvadurai PA, Parker JM, Glaser SD (2017) Numerical modeling describing the effects of heterogeneous distributions of asperities on the quasi-static evolution of frictional slip. Rock Mech Rock Engng 50:3323–3335
Selvadurai APS, Selvadurai PA, Suvorov AP (2018) Contact mechanics of a dilatant region located at a compressed elastic interface. Int J Eng Sci 133:144–168
Shi JQ, Durucan S (2016) Near-exponential relationship between effective stress and permeability of porous rocks revealed in Gangi's phenomenological models and application to gas shales. Int J Coal Geol 154–155:111–122
Tang ZC, Liu QS, Xia CC, Song YL, Huang JH, Wang CB (2014) Mechanical model for predicting closure behavior of rock joints under normal stress. Rock Mech Rock Engng 47:2287–2298
Tang ZC, Jiao YY, Wong LNY (2017) Theoretical model with multi-asperity interaction for the closure behavior of rock joint. Int J Rock Mech Min Sci 97:15–23
Vogler D, Settgast RR, Annavarapu C, Madonna C, Bayer P, Amann F (2018) Experiments and simulations of fully hydro-mechanically coupled response of rough fractures exposed to high-pressure fluid injection. J Geophys Res 123:1186–1200
Willner K (2003) Kontinuums- und kontaktmechanik. Springer-Verlag, Berlin, Synthetische und analytische Darstellung
Wriggers P, Laursen TA (2007) Computational contact mechanics. Springer-Verlag, Berlin